Infrared fixed point of SU(2) gauge theory with six flavors

Leino, Viljami

2018-06-05

Leino , V , Rummukainen , K , Suorsa , J , Tuominen , K & Tähtinen , S 2018 , ' Infrared fixed point of SU(2) gauge theory with six flavors ' , Physical Review D , vol. 97 , no. 11 , 114501 . https://doi.org/10.1103/PhysRevD.97.114501

http://hdl.handle.net/10138/236643
https://doi.org/10.1103/PhysRevD.97.114501

Infrared fixed point of SU(2) gauge theory with six flavors

Viljami Leino,[1,2,*] Kari Rummukainen,[1,2,†] Joni Suorsa,[1,2,‡] Kimmo Tuominen,[1,2,§] and Sara Tähtinen[1,2,‖]
[1]Department of Physics, University of Helsinki, P.O. Box 64, FI-00014 Helsinki, Finland
[2]Helsinki Institute of Physics, P.O. Box 64, FI-00014 Helsinki, Finland

(Received 2 August 2017; revised manuscript received 23 March 2018; published 5 June 2018)

We compute the running of the coupling in SU(2) gauge theory with six fermions in the fundamental representation of the gauge group. We find strong evidence that this theory has an infrared stable fixed point at strong coupling and measure also the anomalous dimension of the fermion mass operator at the fixed point. This theory therefore likely lies close to the boundary of the conformal window and will display novel infrared dynamics if coupled with the electroweak sector of the Standard Model.

DOI: 10.1103/PhysRevD.97.114501

I. INTRODUCTION

Determination of the vacuum phase of an SU(N) gauge theory as a function of the number of massless flavors of Dirac fermions, N_f, and their representations presents a challenge for our basic understanding of gauge theory dynamics at strong coupling. A lot of effort in the field of lattice gauge theory has been devoted to address the existence and properties of the infrared fixed point (IRFP), which appears when N_f is between a critical lower limit N_f^{crit} and the loss of asymptotic freedom. The bounds depend on N and the fermion representation. For recent reviews, see Refs. [1–3]. A much-studied benchmark case is SU(2) gauge theory with two Dirac fermions in the adjoint representation [4–18], where the results indicate the existence of an IRFP.

In SU(2) gauge theory with fermions in the fundamental representation, the precise dependence on N_f remains uncertain, despite a large number of recent studies on the lattice [19–24]. The upper edge of the conformal window is robust: the asymptotic freedom is lost at $N_f = 11$, where the one-loop β-function coefficient changes sign. Just below the upper edge, at ten flavors, the theory has a perturbatively stable Banks-Zaks type infrared fixed point [25], which has also been observed on the lattice [21]. Recently, simulations of the eight flavor theory have also shown the existence of a fixed point [24]. On the other hand, the theory with $N_f = 2$ is well below the conformal window and breaks the chiral symmetry according to the expected pattern, and the theory with $N_f = 4$ is expected to fall within this category as well [21]. However, for $N_f = 6$, the previous results remain so far inconclusive [20–23].

In perturbation theory, the β-function is known up to five-loop order in the $\overline{\mathrm{MS}}$ scheme [26]. In SU(2) gauge theory with $N_f = 6$ fundamental representation fermions, the β-function has a nontrival zero (i.e., an IRFP) up to four-loop order. In the five-loop expansion of the β-function, the IRFP vanishes. Similar behavior has been observed in SU(3) with $N_f = 12$ [27]. However, the SU(2) five-loop β-function shows peculiar behavior as N_f is varied: it predicts an IRFP in two disconnected domains, at $3.0 \lesssim N_f \lesssim 5.8$ and $8.6 \lesssim N_f < 11$. $N_f = 6$ lies between these ranges. This kind of behavior is clearly unphysical and shows that perturbation theory cannot be quantitatively relied upon when the fixed point appears at strong coupling.

In this article, we give strong evidence that the six flavor theory indeed has an IRFP at strong coupling. The result is based on thorough state-of-the-art measurements of the running coupling and the anomalous dimension of the fermion mass operator. We use the Hypercubic truncated stout (HEX) smeared Wilson-clover fermion lattice action and measure the coupling using the Yang-Mills gradient flow [28,29] in conjunction with the finite volume step scaling function with Dirichlet ("Schrödinger functional") boundary conditions [30]. The value of the coupling at the IRFP, g_*^2, is scheme dependent and hence depends on the gradient flow time. With our benchmark scheme, we find $g_*^2 = 14.5(4)^{+0.4}_{-1.2}$ with statistical and systematic errors.

We also measure two scheme-independent quantities at the IRFP: the mass anomalous dimension γ_m^* and the leading irrelevant critical exponent γ_g^*, which gives the slope of the β-function at the IRFP. The mass anomalous

*viljami.leino@helsinki.fi
†kari.rummukainen@helsinki.fi
‡joni.suorsa@helsinki.fi
§kimmo.i.tuominen@helsinki.fi
‖sara.tahtinen@helsinki.fi

dimension is measured using two different methods: the mass step scaling method [31] and the Dirac operator spectral density method [32]. At the fixed point, we observe $\gamma_m^* = 0.283(2)^{+0.01}_{-0.01}$. The slope of the β-function is directly measurable from the step scaling function of the coupling, obtaining $\gamma_g^* = 0.648(97)^{+0.16}_{-0.1}$. In contrast to the value of the fixed point coupling, we observe that γ_g^* remains independent of the gradient flow time, in accord with the scheme independence of this quantity.

This paper is structured as follows. In Sec. II, we define the model and outline the simulation methods. The numerical results are presented for running coupling, leading irrelevant exponent, and mass anomalous dimension, in Secs. III–V respectively. In Sec. VI, we present our conclusions.

II. LATTICE IMPLEMENTATION

The model we use and the algorithmic details we apply are described in detail in Refs. [17,24], and our discussion here will be brief so that we can then focus on the results we obtain in the case of $N_f = 6$. The model is defined by the lattice action

$$S = (1 - c_g)S_G(U) + c_g S_G(V) + S_F(V) + c_{\mathrm{SW}}\delta S_{\mathrm{SW}}(V).$$

The smeared gauge link V is defined by hypercubic truncated stout smearing (HEX smearing) [33], and we mix smeared, $S_G(V)$, and unsmeared, $S_G(U)$, Wilson gauge actions with mixing parameter $c_g = 0.5$. This partial smearing allows us to reach significantly larger couplings by avoiding the unphysical bulk phase transition in the region of interest of the parameter space [34]. We use clover Wilson fermion action with the Sheikholeslami-Wohlert coefficient set to tree-level value of unity, $c_{\mathrm{SW}} = 1$, which is the standard choice for smeared clover fermions. We have verified that this value is very close to the true nonperturbatively fixed c_{SW} coefficient, canceling most of the $O(a)$ errors.

On a lattice of size L^4, we use Dirichlet boundary conditions at the temporal boundaries $x_0 = 0, L$ by setting the gauge link matrices $U = V = 1$ and the fermion fields to zero. The spatial boundaries are periodic. These boundary conditions enable simulations at vanishing fermion mass and allow the mass anomalous dimension to be measured using the same configurations as for the running coupling.

We run our simulations using the hybrid Monte Carlo algorithm with a second order Omelyan integrator [35,36] and chronological initial values for the fermion matrix inversions [37]. We tune the step length to have an acceptance rate larger than 85%. We run the simulations with bare couplings varying within the range

$$\beta_L \equiv 4/g_0^2 \in [0.5, 8] \tag{1}$$

and tune the hopping parameter $\kappa_c(\beta_L)$ so that the absolute value of the fermion mass determined via the axial Ward identity [38] is less than 10^{-5} at lattices of size 24^4. The same critical hopping parameter values are used for all the lattice sizes, and for each β_L [and corresponding $\kappa_c(\beta_L)$]. The critical hopping parameters are available in the Table III. We use lattices of sizes $L = 8$, 10, 12, 16, 18, 20, 24, and 30, chosen to allow step scaling with either $s = 2$ or $s = 3/2$. For our analysis, we choose $s = 3/2$ as it includes more pairs within the larger lattices. We generate $(5\text{–}100) \times 10^3$ trajectories for each combination of β_L and L. For the exact number of trajectories used, see Table IV.

To define the running coupling, we apply the Yang-Mills gradient flow method [28–30]. This method defines a flow that smooths the gauge fields and removes UV divergences and automatically renormalizes gauge invariant objects [39]. The method is set up by introducing a fictitious flow time t and studying the evolution of the flow gauge field $B_\mu(x, t)$ according to the flow equation

$$\partial_t B_\mu = D_\nu G_{\nu\mu}, \tag{2}$$

where $G_{\mu\nu}(x; t)$ is the field strength of the flow field B_μ and $D_\mu = \partial_\mu + [B_\mu, \cdot]$. The initial condition is $B_\mu(x; t = 0) = A_\mu(x)$, where A_μ is the original continuum gauge field. In the lattice formulation, the (unsmeared) lattice link variable U replaces the continuum flow field, which we then evolve using either the tree-level improved Lüscher-Weisz pure gauge action (LW) [40] or the Wilson plaquette gauge action (W). In the continuum limit, these should yield identical results, providing a check of the reliability of the limit.

The coupling at scale $\mu = 1/\sqrt{8t}$ [41] is defined via energy measurement as

$$g_{\mathrm{GF}}^2(\mu) = \mathcal{N}^{-1} t^2 \langle E(t + \tau_0 a^2)\rangle|_{x_0 = L/2, t = 1/8\mu^2}, \tag{3}$$

where a is the lattice spacing. The shift parameter τ_0 is introduced to reduce the $\mathcal{O}(a^2)$ discretization effects caused by the flow [42] and can be numerically estimated during the analysis. The normalization factor $\mathcal{N}$ for the chosen boundary conditions has been calculated in Ref. [43] to match the $\overline{\mathrm{MS}}$ coupling in the tree level. As the translation symmetry is broken by the chosen boundary conditions, the coupling g_{GF}^2 is measured only on the central time slice $x_0 = L/2$. To quantify the effects of different discretizations, we measure the energy density $E(t)$ using both symmetric clover and simple plaquette discretizations of the flow.

In order to limit the scale into a regime where both lattice artifacts and finite volume effects are minimized, we relate the lattice and the renormalization scales by defining a dimensionless parameter c_t such that $\mu^{-1} = c_t L = \sqrt{8t}$ as described in Refs. [43,44]. The chosen boundary conditions

have reasonably small cutoff effects and statistical variance within the range of $c_t = 0.3$–0.5 [43]. The value of this parameter defines the renormalization scheme.

III. EVOLUTION OF THE COUPLING

Our "benchmark" set of results presented here is obtained with the gradient flow Eq. (2) evolved with LW, the clover definition of energy density Eq. (3), and $c_t = 0.3$. In order to estimate systematic errors, we vary discretizations of the flow and the observable and parameter values of the flow. The raw data are available in Tables V–XII.

The measured couplings with the aforementioned parameters are shown in the top panel of Fig. 1. It is clear from the figure that the finite volume effects become substantial on smaller lattices as the coupling grows larger.

To quantify the running of the coupling, we use the finite volume step scaling function [45],

$$\Sigma(u, L/a, s) = g^2_{\rm GF}(g_0, sL/a)|_{g^2_{\rm GF}(g_0, L/a)=u}, \qquad (4)$$

which describes the change of the measured coupling when the linear size of the system is increased from L to sL. The step scaling obtained from the data in Fig. 1 is shown in Fig. 2, using a scaling factor $s = 3/2$, that is, pairs of lattices with $L/a = 8$–12, 12–18, 16–24, and 20–30. At the smallest volume pair $L/a = 8$–12, the step scaling deviates significantly from the others and will be excluded from the continuum analysis. The rest of the volume pairs are observed to follow the scheme-independent two-loop curve in the weak coupling region up to $g^2_{\rm GF} \sim 6$, after which the measured step scaling function deviates toward an IRFP around $g^2_{\rm GF} \sim 14$. Although the higher-loop $\overline{\rm MS}$ results are scheme dependent and cannot be directly compared with our result, we show them for comparison.

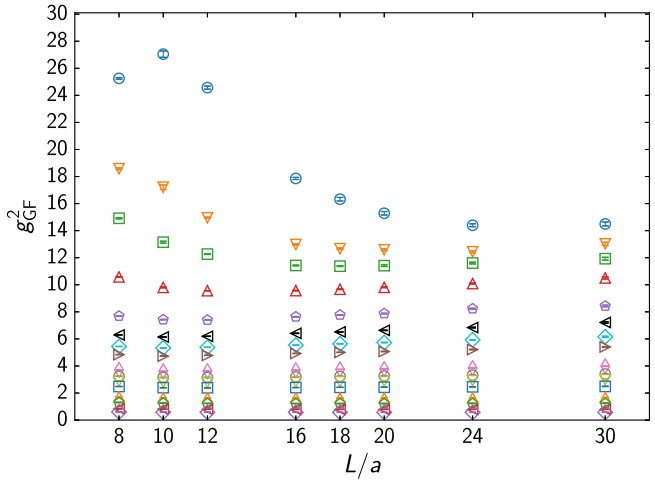

FIG. 1. The gradient flow coupling Eq. (3) measured at each β_L and L/a using the benchmark set of parameters (LW flow action, clover definition of field strength, $c_t = 0.3$).

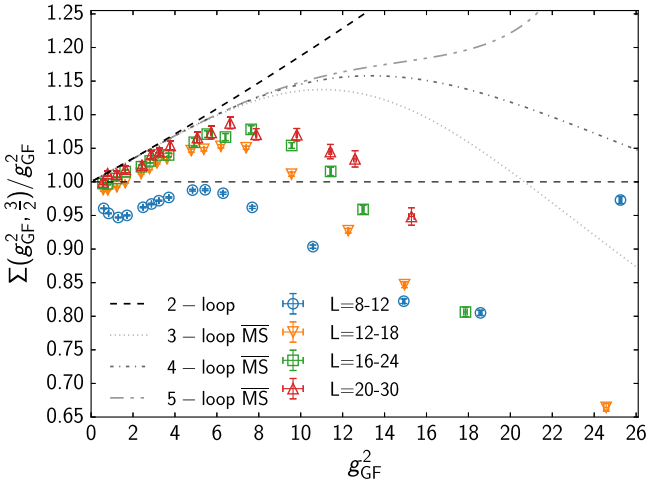

FIG. 2. The lattice step scaling function Eq. (4) obtained from the data in Fig. 1.

For the continuum limit $\sigma(g^2_{\rm GF})$ of the step scaling function, we use the extrapolating function

$$\Sigma(g^2_{\rm GF}, L/a) = \sigma(g^2_{\rm GF}) + c(g^2_{\rm GF})(a/L)^2. \qquad (5)$$

At weak coupling, the cutoff effects are regulated by the proximity of the ultraviolet fixed point, and the lowest order discretization effects of the Wilson-clover action are expected to be of order $\mathcal{O}(a^2)$, motivating the use of Eq. (5).

As will be seen below, at small couplings, the $O(a^2/L^2)$ extrapolation works quite well. However, at large couplings, the range of volumes available to us and the accuracy of measurements are not sufficient to verify this. Using staggered fermions and much larger volumes, it has been observed that in SU(3) theory with $N_f = 12$ fundamental fermions including $O(a^4/L^4)$ effects can affect the continuum limit at a 10% level [46].

At large coupling, so long as the coupling remains below the possible IRFP, the continuum limit is ultimately reached at the UV fixed point. However, due to the smallness of the β-function, this would require astronomically large scale hierarchy between the lattice size L and lattice spacing a and hence is impossible to observe in simulations. Nevertheless, if the anomalous exponents of the fields remain small near the infrared fixed point, one can assume that the power counting of operators is applicable and the cutoff effects (dominated by dimension-6 operators) decrease with a power of the lattice spacing a. The naive a^2 behavior may be modified by anomalous exponents, though. In Sec. V, we observe that the mass anomalous dimension at the IRFP remains relatively small, $\gamma_m \approx 0.28$, suggesting that the a^2 behavior in Eq. (5) may also receive only minor corrections. The available range in our data does not allow us to numerically determine differences

TABLE I. χ^2/d.o.f. of the fit (6) at different L/a and c_t.

c_t	L = 8a	L = 12a	L = 16a	L = 18a	L = 20a	L = 24a	L = 30a
0.3	1.3	0.5	1.0	1.1	0.9	1.5	1.5
0.35	12	0.4	0.6	0.8	0.9	1.3	1.4
0.4	9.3	0.7	0.4	0.7	1.1	1.2	1.6
0.45	8.6	1.1	0.5	1.1	1.4	1.1	1.9

from Eq. (5), and hence we use it at all couplings. Near the IRFP, we indeed observe that the continuum limit becomes somewhat less robust, which is taken into account in our systematic error estimation.

In order to determine the continuum limit of the step scaling function, we need the measurements of the step scaling at constant value of the coupling. However, in practice, the simulations are carried out at a fixed set of bare lattice couplings which does not correspond to same value of g^2_{GF} when a/L is varied. Hence, we adopt the customary interpolation procedure of the measured couplings to intermediate couplings. We do this using a polynomial fit,[1]

$$g^2_{\mathrm{GF}}(g_0, a/L) = g_0^2\left(1 + \sum_{i=1}^{m} a_i g_0^{2i}\right), \tag{6}$$

where we use $m = 10$ for lattices smaller than $L = 16$ and $m = 9$ for the larger lattices. With this choice, we obtain the χ^2/d.o.f.'s reported in Table I for each used c_t and in Table XVI for each used discretization. We study the robustness of the fits by repeating the analysis with m decreased by 1. While this choice increases the χ^2/d.o.f., the results stay compatible with those obtained with larger m.

In Fig. 3, we show the continuum limit extrapolation of the step scaling function when g^2_{GF} is varied from weak to strong coupling, obtained using Luscher-Weisz or Wilson flow actions and clover or plaquette field strength observables. At small couplings, the continuum limit is very well under control: different discretizations extrapolate very close to the same value. At couplings $g^2_{\mathrm{GF}} \gtrsim 10$, the continuum limits start to show a few percent scatter. This is taken into account in the systematic uncertainties of the final results.

The τ_0-correction parameter in (3) can be tuned to reduce most of the $O(a^2)$ errors from the continuum limit extrapolation of the step scaling function Eq. (5). The parameter τ_0 should have a small effect in the continuum extrapolation, so long as it is not too large [47]. In practice, we have observed that τ_0 which depends logarithmically on g^2_{GF} works well at small coupling [24]. With $c_t = 0.3$, the Luscher-Weisz flow action, and clover field strength observable, we use

$$\tau_0 = 0.025 \log(1 + 2g^2_{\mathrm{GF}}), \tag{7}$$

which makes the interpolation errors almost vanish at $g^2_{\mathrm{GF}} \lesssim 10$, as can be observed in Fig. 3. At larger couplings, τ_0 correction cannot remove $O(a^2)$ significantly without ruining the continuum limit. We note that in order to have a consistent $\mathcal{O}(a^2)$ shift in the step scaling analysis the τ_0 correction should be a function of g^2_{GF} instead of the bare

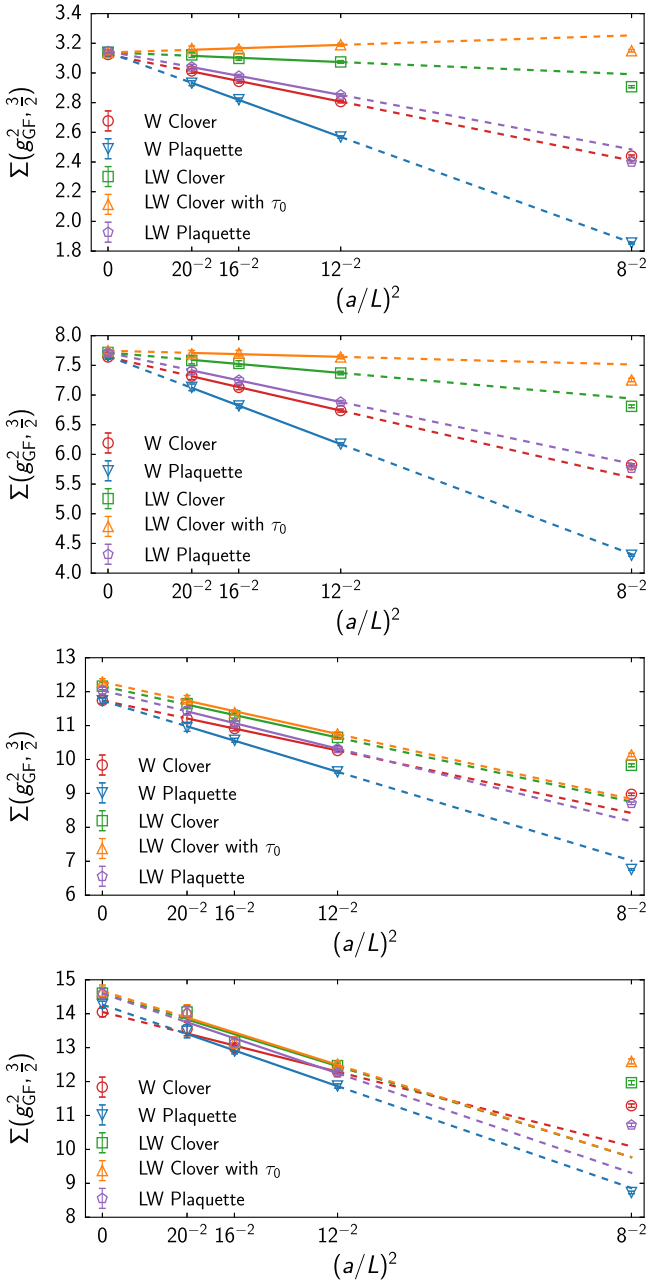

FIG. 3. The effects of the choice of the W and the LW flow actions, the clover and the plaquette field strength observables, and the τ_0 correction Eq. (7) on the continuum limit of the step scaling function Eq. (5) for $c_t = 0.3$, measured at couplings (from top to bottom) $g^2_{\mathrm{GF}} = 3$, $g^2_{\mathrm{GF}} = 7$, $g^2_{\mathrm{GF}} = 11$, and $g^2_{\mathrm{GF}} = 14.5$.

[1]A rational interpolating function is another choice used in the literature [21,24]. However, in our case, this did not offer any improvement.

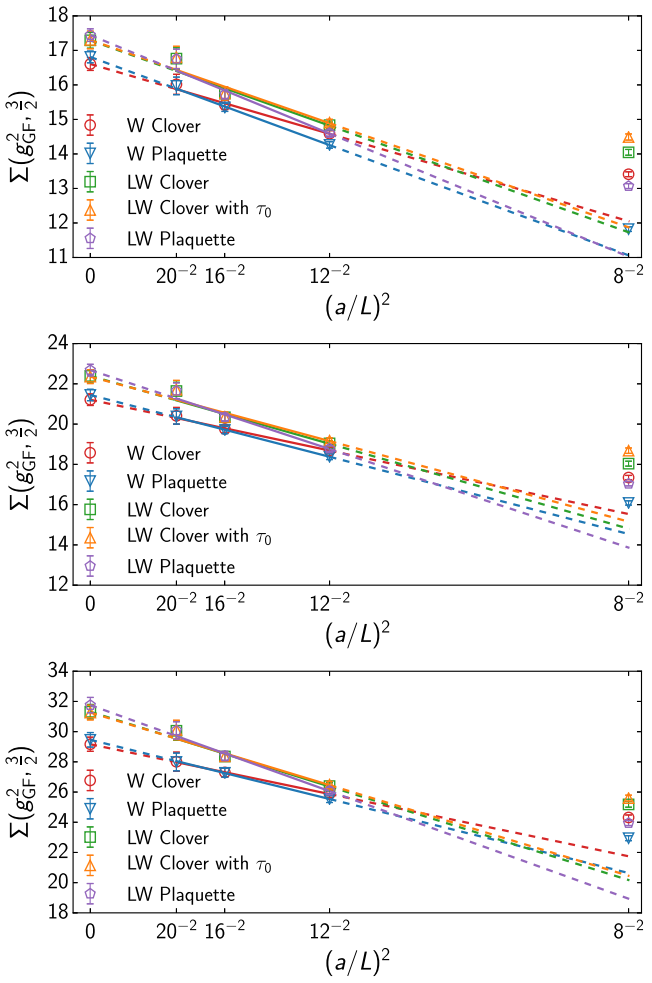

FIG. 4. From top to bottom: Same as Fig 3 but with $c_t = 0.35$, $c_t = 0.4$, and $c_t = 0.45$ measured at their respective IRFP's given in Table II.

coupling g_0^2 [30]. Because adjusting τ_0 changes the value of the measured $g^2_{\rm GF}$, the final value of τ_0 is found by iterating Eqs. (3) and (7), starting from the initial value $g^2_{\rm GF} = g_0^2$.

In Fig. 4, we show the continuum limit of the step scaling at $c_t = 0.35$, 0.4, and 0.45, evaluated at the IRFP of each c_t. The couplings $g^2_{\rm GF} = g^2_*$ at the fixed point are shown in Table II. Because different c_t values correspond to different coupling constant schemes, the values of g^2_* vary significantly. It is evident that as c_t is increased the difference between the Lüscher-Weisz and Wilson flow actions grows, contributing to increasing systematic errors.

TABLE II. Measured couplings and critical exponents with different choices of parameter c_t. The error shown in parentheses is the statistical uncertainty, and the super- and subscripts are the systematic errors due to different discretizations of the gradient flow and the field strength observables.

	$c_t = 0.3$	0.35	0.4	0.45
g^2_*	$14.5(4)^{+0.4}_{-1.2}$	$17.1(5)^{+0.8}_{-1.3}$	$22.2(6)^{+1.3}_{-2.5}$	$31(1)^{+2}_{-18}$
γ^*_g	$0.648(97)^{+0.16}_{-0.1}$	$0.71(12)^{+0.17}_{-0.11}$	$0.73(10)^{+0.11}_{-0.18}$	$0.75(12)^{+0.12}_{-0.61}$

Finally, in Fig. 5, we show the continuum limit of the step scaling across the full range of $g^2_{\rm GF}$ at $c_t = 0.3$, 0.35, and 0.4. The scheme-independent two-loop result and the scheme-dependent three- and four-loop $\overline{\rm MS}$ results are shown as references, while the five-loop curve from Fig. 2 is not shown here as it would mostly be outside the figure. The error bands include the statistical errors and systematic uncertainty arising from different interpolating polynomials, Eq. (6). It is evident that as c_t increases the reliability of the continuum limit extrapolation decreases,

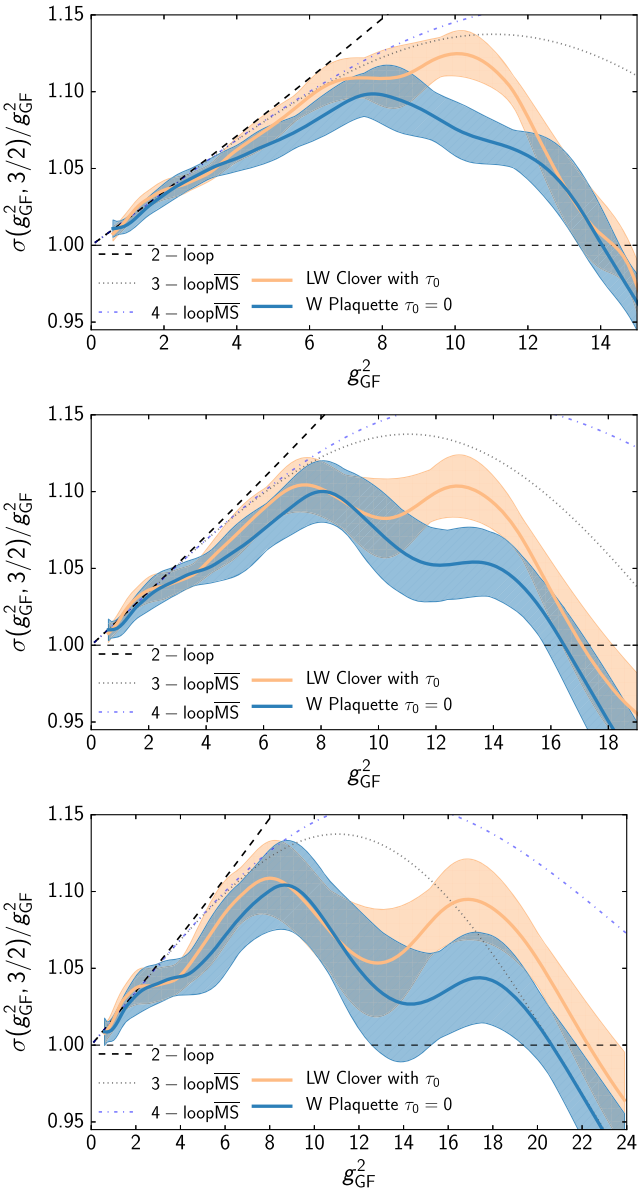

FIG. 5. From top to bottom: The continuum limit of the interpolated step scaling function at $c_t = 0.3$, $c_t = 0.35$, and $c_t = 0.4$, using discretizations which give the smallest and largest results for the step scaling function.

and already at $c_t = 0.4$, the final result has a clearly unphysical strong "wavy" structure. This is caused by the use of the polynomial interpolation functions in Eq (6). We note that if we would use polynomials of smaller degree [for example, $m = 8$ in (6)] the wavy structure would be strongly reduced and error bands would be much narrower; however, the χ^2/d.o.f. values would not be acceptable.

Each value of c_t corresponds to different coupling constant schemes, and the value of the fixed point coupling strongly depends on the value of c_t. The location of the fixed point for each c_t is reported in Table II and individually for all discretizations of the flow in Table XIV in the Appendix. The first error is the statistical uncertainty, and the second error estimates systematic effects by including the full range of different discretization choices that were present in Fig. 3. For our benchmark value $c_t = 0.3$, we find that our continuum extrapolated results are compatible within 1σ level with respect to all these effects except in the interval $g^2_{\mathrm{GF}} \in [8, 12]$ where LW and W evolved flows disagree slightly. In this case, the fixed point coupling has the value $g^2_* = 14.5(4)^{+0.4}_{-1.2}$.

IV. LEADING IRRELEVANT CRITICAL EXPONENT

We can also obtain the leading irrelevant exponent γ^*_g at the fixed point, defined by the slope of the β-function at the IRFP. This quantity is scheme independent and thus should not depend on c_t.

In the proximity of the fixed point, we can approximate the β-function as

$$\beta(g) = -\mu \frac{dg^2}{d\mu} \approx \gamma^*_g (g^2 - g^2_*)$$
$$\approx \bar{\beta}(g) \equiv \frac{g}{2\ln(s)} \left(1 - \frac{\sigma(g^2, s)}{g^2}\right). \quad (8)$$

Measuring the slope of the step scaling function $\sigma(g^2)$ around the fixed point gives the exponent $\gamma^*_g = 0.648(97)^{+0.16}_{-0.1}$ at $c_t = 0.3$; the results with other c_t are shown in Table II. While there is noticeable variance between different discretizations, as indicated by the second set of errors, the result is compatible with the recent scheme-independent estimate of $\gamma^*_g = 0.6515$ in Refs. [48,49]. The results obtained with different discretizations are shown individually in Table XV. When c_t is varied, the value of γ^*_g remains constant within errors, in accord with the scheme independence of this quantity.

The results obtained above rely on the accurate continuum limit of the step scaling function $\sigma(g^2)$. However, as discussed in Sec. III, the continuum limit may be in effect somewhat differently at the close proximity of the IRFP. We can verify the consistency of the results by using a finite size scaling method developed in Refs. [50–53] to get an alternative measurement of γ^*_g. In the close proximity of the IRFP, by integrating (8), we obtain a finite size scaling relation between lattices of size L_{ref} and L [52]:

$$g^2_{\mathrm{GF}}(\beta_L, L) - g^2_* = [g^2_{\mathrm{GF}}(\beta_L, L_{\mathrm{ref}}) - g^2_*] \left(\frac{L_{\mathrm{ref}}}{L}\right)^{\gamma^*_g}. \quad (9)$$

This equation relies on the evolution of the coupling toward the fixed point as the lattice size is increased from L_{ref} to L. Hence, it cannot be used exactly at the fixed point where there is no evolution, but only in some environment around it. We note that this also assumes vanishing discretization artifacts, and thus it can be used only if the lattices are already close enough to the continuum (L large).

In Fig. 6, we show the fit to Eq. (9) to individual measurements of g^2_{GF} at $\beta_L \leq 0.8$, corresponding to measurements which are close to the fixed point. A good fit to Eq. (9) is obtained if we choose $L_{\mathrm{ref}}/a \geq 18$, allowing us to extract an estimate for γ^*_g.

Instead of using individual measurements, we use the interpolated values of $g^2_{\mathrm{GF}}(\beta_L, L)$, because this allows us to freely tune the value of β_L. In Fig. 7, we show the resulting γ^*_g from fits to Eq. (9), plotted as functions of $g^2_{\mathrm{ref}} \equiv g^2_{\mathrm{GF}}(\beta_L, L_{\mathrm{ref}})$. The red lines correspond to the values given in Table XV, measured from the slope of the step scaling function. The shaded error bands correspond to statistical errors while keeping the values of g^2_* fixed to central values in Table XIV, and the dashed lines show the variation of the result if we allow g^2_* to vary within the statistical error range.

The resulting γ^*_g is expected to be close to the true γ^*_g only in close proximity of the IRFP. However, too close to the IRFP, Eq. (9) becomes unstable, which is indicated by a sudden drop in the γ^*_g measurements. Indeed, at $g^2_{\mathrm{ref}} \approx 12$, we observe the $c_t = 0.3$ case to give γ^*_g, which is in agreement with the one obtained from the slope of the β-function. At small g^2_{ref}, the measurement of γ^*_g using Eq. (9) approaches zero.

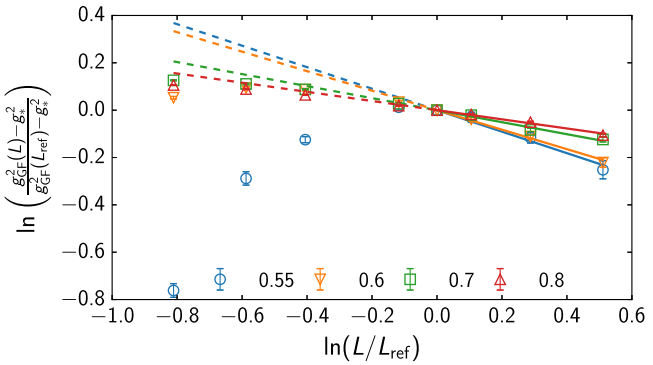

FIG. 6. Fit to function (9) for measured couplings $g^2_{\mathrm{GF}}(\beta_L, L)$ at $\beta_L = 0.55 \ldots 0.8$ at $c_t = 0.3$, using $L_{\mathrm{ref}}/a = 18$.

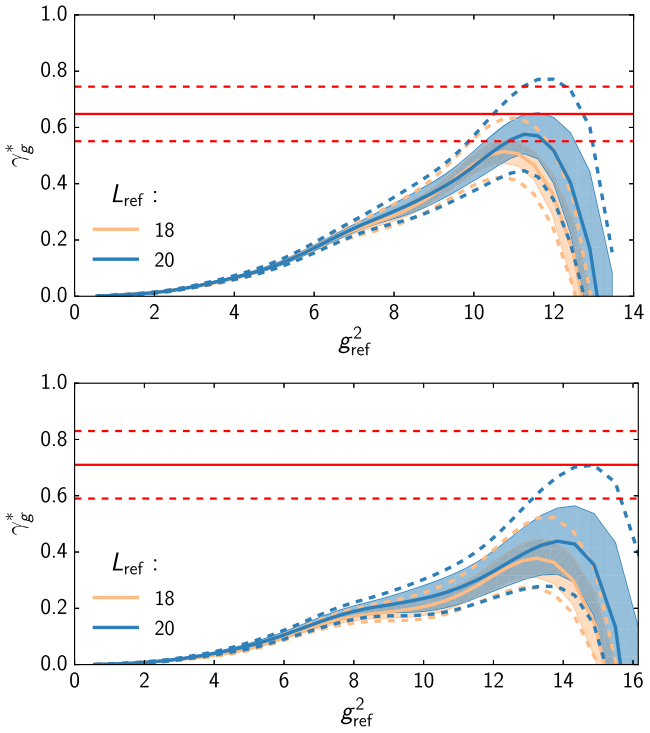

FIG. 7. Fit to function (9) for all couplings $g^2_{\rm GF}(\beta_L, L_{\rm ref})$ with the chosen set of discretizations: (top) at $c_t = 0.3$ and (bottom) at $c_t = 0.35$. The shaded bands indicate the statistical errors for g^2_* being the measured value, and dashed lines indicate how the result changes when g^2_* is varied within its statistical errors.

V. ANOMALOUS DIMENSION OF THE MASS OPERATOR

In order to measure the anomalous dimension of the fermion mass operator γ^*_m, we use two different methods, the mass step scaling method and the spectral density method. In the step scaling method, we measure γ_m from the running of the pseudoscalar density renormalization constant [31,54]

$$Z_P(g_0, L) = \frac{\sqrt{2f_1}}{f_P(L/2)}, \tag{10}$$

where f_P and f_1 are pseudoscalar current densities defined explicitly in e.g., Refs. [24,38]. The mass step scaling function is defined as [31]

$$\Sigma_P(u, s, L/a) = \left.\frac{Z_P(g_0, sL/a)}{Z_P(g_0, L/a)}\right|_{g^2_{\rm GF}(g_0, L/a)=u}. \tag{11}$$

As in the case of the coupling, we choose $s = 3/2$. The continuum limit $\sigma_P(u, s)$ is obtained by interpolating the measured Z_p by eighth order polynomials and assuming $\mathcal{O}(a^2)$ errors. The mass anomalous dimension is then obtained as [54]

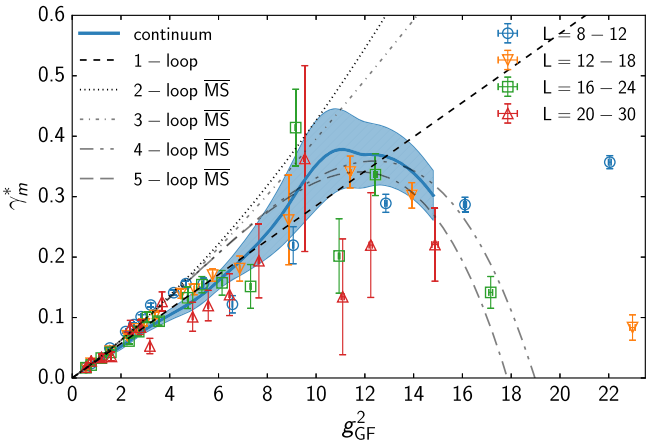

FIG. 8. The mass anomalous dimension as a function of the gradient flow coupling constant obtained using the mass step scaling function and its continuum limit. The results become unstable at large couplings.

$$\gamma^*_m(u) = -\frac{\log \sigma_P(u, s)}{\log s}. \tag{12}$$

The results are shown in Fig. 8, and the raw data are given in Table XIII. The method gives results comparable to one-loop perturbation theory predictions at small gauge coupling $g^2_{\rm GF}$. While the higher-loop $\overline{\rm MS}$ expansions [55,56] are scheme dependent and cannot be directly compared to our results, it is nevertheless comforting to observe comparable behavior between our result to the four- and five-loop behavior. However, the method becomes unstable at large coupling, which implies that at the fixed point $g^2_* \approx 14.5$ the continuum limit cannot be trusted.

The second way to measure γ_m is based on the fact that the it also determines the scaling of the spectral density of the massless Dirac operator. The explicit calculation of the eigenvalue distribution is prohibitively costly, but the stochastic methods [57] have made it possible to determine the mass anomalous dimension from the scaling of the mode number of the Dirac operator [32]. The mode number is known to follow a scaling behavior.

$$\nu(\Lambda) \propto \Lambda^{4/(1+\gamma^*_m)}, \tag{13}$$

in some energy range between the infrared and the ultraviolet in the vicinity of a fixed point. Here, γ^*_m is the mass anomalous dimension γ_m at the fixed point.

We calculate the mode number per unit volume of Eq. (13) by using

$$\nu(\Lambda) = \lim_{V\to\infty} \frac{1}{V} \langle {\rm tr}\mathbb{P}(\Lambda)\rangle, \tag{14}$$

where the operator $\mathbb{P}(\Lambda)$ projects from the full eigenspace of $M = m^2 - \not{D}^2$ to the eigenspace of eigenvalues smaller than Λ^2. The trace is evaluated stochastically [57] and fitted to the power law behavior of Eq. (13). However, the energy

range where this power law behavior holds is not known beforehand and needs to be determined by observing the quality of the fit in a given range.

We use $L/a = 24$ lattices from the step scaling analysis and take 12 to 20 well-separated configurations for each value of the gauge coupling. We calculate the mode number for 90 values of Λ^2 ranging from 10^{-3} to 0.3. The results are then fitted to Eq. (13). The fit range is determined by varying its lower and the upper limits and observing the stability and the quality of the fit. As a cross-reference at weak coupling, the fitted value of γ_m^* and the value obtained with the step scaling method are compared.

In Fig. 9, we plot the mode number divided by the fourth power of the eigenvalue scale, where the fit range and the fit function of Eq. (13) are shown overlaid in red. According to Eq. (13), in the proximity of the fixed point, the infrared behavior should be a power law in the absence of lattice artifacts. We observe this at strongest couplings; however, at small couplings, the low eigenvalues appear in discrete energies, which manifests as the bumps in the mode number curve, making the power law less evident. To illustrate the evolution of the mass anomalous dimension, we use the same fit range for both weak and strong couplings.

The final result of the spectral density method is shown in Fig 10, where the mass anomalous dimension γ_m^*, obtained by fitting the data with Eq. (13), is shown as a function of the gauge coupling g^2_{GF}. The shaded band illustrates the uncertainty resulting from varying the upper and lower limits of the fit range by ∼50%. The largest uncertainty arises at small gauge couplings, where the bumps in the data cause the changes in the fit range to change the fit dramatically. The error band of Fig. 10 becomes narrower toward the larger couplings as the ensembles near the IRFP are less sensitive to variations of the fit range.

At the fixed point $g_*^2 = 14.5$, we obtain $\gamma_m^* = 0.283(2)^{+0.01}_{-0.01}$. However, this result is obtained at fixed lattice size $L/a = 24$. A proper continuum limit requires extrapolation to infinite L, but at smaller L/a, the finite size effects make the usable range for the power law fit too narrow.

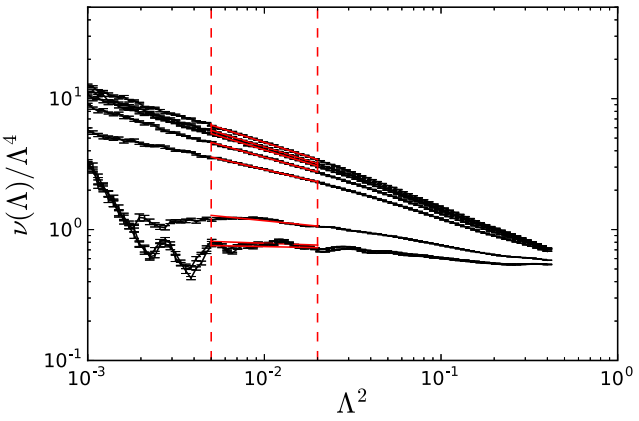

FIG. 9. The mode number divided by $a^4\Lambda^4$ as a function of $a^2\Lambda^2$ on a $L/a = 24$ lattice. The dashed red lines indicate the chosen fit range, and the red solid lines indicate the fit function. The fit ranges were varied around these chosen regions. The curves are in a descending gauge coupling order.

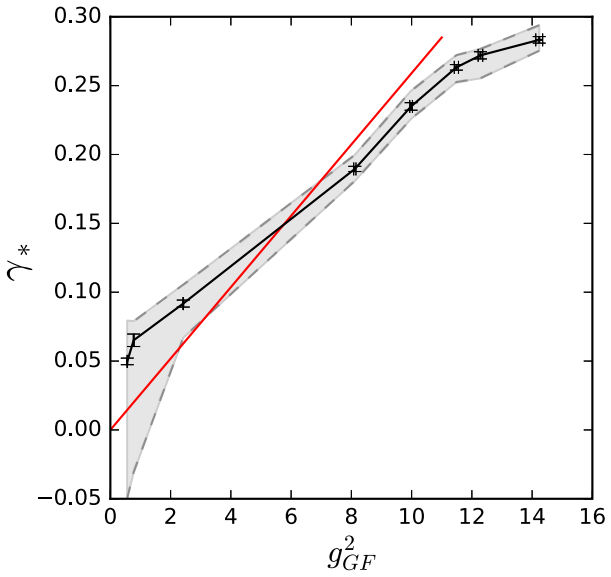

FIG. 10. The value of γ_m^* obtained by fitting Eq. (13) to the data in Fig. 9 is shown with black points and the one-loop perturbative result with a red line. The shaded regions are estimates for reasonable ranges of values obtainable using the method and were obtained by varying the fit range shown in Fig. 9 slightly.

Interestingly, the mass step scaling method and the spectral density method complement each other: while the mass step scaling is stable and accurate at weak couplings, where the spectral density method fails, at strong coupling, the roles are reversed.

VI. CONCLUSIONS

We have studied the running coupling in the SU(2) lattice gauge theory with six fermions in the fundamental representation. The gradient flow algorithm with Dirichlet boundaries was shown to provide robust results on the large coupling behavior of this theory giving a result consistent with the existence of IRFP at $g_*^2 = 14.5(4)^{+0.4}_{-1.2}$ in our benchmark scheme. The scheme-independent slope of the β-function at the IRFP was measured to be $\gamma_g^* = 0.648(97)^{+0.16}_{-0.1}$.

We also determined the mass anomalous dimension γ_m in this theory using the spectral density method and the mass step scaling method. The step scaling method gives results compatible with perturbation theory at weak coupling. At intermediate couplings, the step scaling method can be matched on the results from the spectral density method which remain stable in the vicinity of the fixed point where the step scaling computation breaks down. With the spectral density method, we estimated the mass anomalous dimension at the fixed point as $\gamma_m^* = 0.283(2)^{+0.01}_{-0.01}$, albeit a proper continuum limit is still lacking.

Our results are consistent with the existence of a strong coupling IRFP and indicate that the SU(2) gauge theory with six fermion flavors in the fundamental representation is within the conformal window. The theory likely is near the lower boundary of the conformal window, which makes it an interesting candidate for beyond the Standard Model theories: when coupled with the electroweak gauge currents, the chiral symmetries are explicitly broken, and the theory is pulled outside the conformal window and may constitute a concrete example of a walking technicolor theory.

ACKNOWLEDGMENTS

This work is supported by the Academy of Finland Grants No. 267286 and No. 267842. V. L. and J. M. S. are supported by the Jenny and Antti Wihuri Foundation, and S. T. is supported by the Magnus Ehrnrooth Foundation. The simulations were performed at the Finnish IT Center for Science, Espoo, Finland.

APPENDIX: TABLES

In this appendix we provide the numerical values of the measurements in tabulated form. In Table III we show the critical hopping parameter values used at each β_L and in Table IV the number of hybrid Monte Carlo trajectories. In Tables V–XIII we show the measured gradient flow couplings g^2_{GF} at different choices for gradient flow parameters, energy density operator and flow action. Table XIV shows the location of the IRFP and Table XV the value of the γ_g^* for each of the discretization choices in Tables V–XIII. Table XVI shows the combined $\chi^2/\mathrm{d.o.f.}$ for the interpolation fits of type shown in Eq. (6).

TABLE III. The measured $\kappa_c(\beta_L)$ at $L/a = 24$ for each β_L.

β_L	κ_c	β_L	κ_c	β_L	κ_c	β_L	κ_c
8	0.125310366353981	2	0.127533813721664	1	0.131448889150607	0.6	0.136438136224601
6	0.125459579958083	1.7	0.128194200995596	0.9	0.132331360707040	0.55	0.137424583321490
4	0.125860459184944	1.5	0.128799165934744	0.8	0.133419041876613	0.53	0.137839481272905
3	0.126367585261215	1.3	0.129603737388233	0.7	0.134765027707880	0.5	0.138504981089103

TABLE IV. Number of trajectories for each β_L and L after thermalization.

β_L	$N(L=8)$	$N(L=10)$	$N(L=12)$	$N(L=16)$	$N(L=18)$	$N(L=20)$	$N(L=24)$	$N(L=30)$
8	81 351	10 849	78 537	8500	6468	11 473	62 574	7383
6	157 185	20 468	89 006	122 197	95 460	40 434	33 845	6098
4	95 516	20 604	84 883	106 793	86 888	41 198	14 031	5963
3	101 614	23 139	88 269	102 191	82 956	39 127	21 475	8520
2	94 905	17 527	82 783	94 976	76 712	35 925	40 449	9146
1.7	93 581	19 990	79 821	92 194	74 062	34 220	36 175	8785
1.5	92 038	19 268	113 427	90 364	70 024	32 955	21 173	10 895
1.3	89 055	18 380	110 383	88 057	69 042	31 553	32 209	12 014
1	85 016	16 659	105 548	75 659	75 037	33 030	19 082	11 730
0.9	100 759	22 780	106 021	77 452	72 799	46 582	47 578	15 254
0.8	78 037	29 807	135 876	95 623	97 127	71 468	42 482	21 425
0.7	130 058	30 235	134 124	90 815	105 578	43 926	20 925	20 403
0.6	126 248	30 284	121 780	146 073	93 686	68 932	62 787	19 478
0.55	131 577	22 127	123 599	103 778	88 999	42 183	28 736	16 607
0.53	137 302	24 401	146 940	84 434	43 674	64 683	29 323	15 825
0.5	128 873	23 648	99 971	86 445	26 464	39 693	23 994	15 355

TABLE V. The measured gradient flow couplings g^2_{GF} with the chosen set of parameters: LW evolved flow, clover definition of energy density, $c_t = 0.3$, and $\tau_0 = 0.025\log(1 + 2 * g^2_{\mathrm{GF}})$. These are the parameters used in most of the work. The statistical errors are counted with the jackknife method.

β_L	$L=8$	$L=10$	$L=12$	$L=16$	$L=18$	$L=20$	$L=24$	$L=30$
8	0.56878(16)	0.5639(5)	0.56447(17)	0.5642(8)	0.5660(14)	0.5660(9)	0.5674(5)	0.5687(19)
6	0.77786(18)	0.7718(5)	0.7718(3)	0.7754(4)	0.7760(5)	0.7776(6)	0.7808(10)	0.792(3)
4	1.1816(3)	1.1736(11)	1.1781(5)	1.1913(6)	1.1960(9)	1.2012(15)	1.212(2)	1.224(5)
3	1.5426(6)	1.5383(14)	1.5546(9)	1.5827(12)	1.5933(16)	1.607(2)	1.630(4)	1.653(7)

(Table continued)

TABLE V. *(Continued)*

β_L	$L=8$	$L=10$	$L=12$	$L=16$	$L=18$	$L=20$	$L=24$	$L=30$
2	2.1936(10)	2.213(3)	2.2591(18)	2.329(2)	2.357(2)	2.379(4)	2.423(5)	2.466(12)
1.7	2.5286(15)	2.559(3)	2.6261(19)	2.726(2)	2.765(4)	2.803(6)	2.863(7)	2.951(16)
1.5	2.8258(14)	2.881(4)	2.956(2)	3.083(3)	3.142(3)	3.184(8)	3.268(9)	3.368(17)
1.3	3.2215(19)	3.295(5)	3.396(3)	3.563(4)	3.638(6)	3.684(9)	3.781(9)	3.93(2)
1	4.163(3)	4.283(6)	4.460(4)	4.730(6)	4.846(9)	4.939(14)	5.11(2)	5.33(3)
0.9	4.665(3)	4.822(9)	5.008(5)	5.317(8)	5.456(12)	5.577(15)	5.82(2)	6.07(4)
0.8	5.383(7)	5.538(14)	5.755(5)	6.145(16)	6.302(14)	6.451(18)	6.70(2)	7.12(5)
0.7	6.570(8)	6.69(2)	6.867(10)	7.314(19)	7.509(15)	7.65(2)	8.06(3)	8.32(6)
0.6	9.06(2)	8.83(3)	8.876(14)	9.16(2)	9.34(2)	9.53(2)	9.88(3)	10.36(7)
0.55	12.86(4)	11.86(7)	11.39(2)	10.94(2)	10.98(2)	11.09(6)	11.37(6)	11.77(10)
0.53	16.10(6)	15.59(16)	13.92(5)	12.43(4)	12.24(5)	12.24(6)	12.19(7)	12.85(12)
0.5	22.04(5)	24.6(2)	22.97(11)	17.16(7)	15.80(12)	14.87(13)	14.12(10)	14.30(14)

TABLE VI. The measured gradient flow couplings g^2_{GF} with otherwise the same parameters as Table V but with $\tau_0 = 0$.

β_L	$L=8$	$L=10$	$L=12$	$L=16$	$L=18$	$L=20$	$L=24$	$L=30$
8	0.60287(17)	0.5851(5)	0.57911(17)	0.5724(8)	0.5724(14)	0.5712(9)	0.5710(5)	0.5711(19)
6	0.83581(19)	0.8078(6)	0.7966(3)	0.7893(4)	0.7869(5)	0.7865(6)	0.7870(10)	0.796(3)
4	1.2955(3)	1.2443(12)	1.2268(5)	1.2189(6)	1.2178(9)	1.2190(15)	1.225(2)	1.232(6)
3	1.7145(6)	1.6456(15)	1.6290(10)	1.6252(12)	1.6271(16)	1.635(2)	1.650(4)	1.665(7)
2	2.4813(11)	2.396(3)	2.3875(18)	2.404(2)	2.417(2)	2.428(4)	2.458(5)	2.488(12)
1.7	2.8793(16)	2.782(3)	2.784(2)	2.819(2)	2.840(4)	2.864(6)	2.907(7)	2.980(16)
1.5	3.2339(15)	3.143(4)	3.143(2)	3.193(3)	3.231(3)	3.257(8)	3.321(9)	3.403(17)
1.3	3.707(2)	3.610(5)	3.621(3)	3.696(4)	3.746(7)	3.773(9)	3.845(9)	3.97(2)
1	4.839(3)	4.725(7)	4.780(4)	4.923(6)	5.002(9)	5.069(14)	5.21(2)	5.40(3)
0.9	5.441(3)	5.332(10)	5.377(5)	5.540(8)	5.638(12)	5.729(15)	5.93(2)	6.15(4)
0.8	6.297(7)	6.139(15)	6.191(6)	6.410(16)	6.518(14)	6.632(18)	6.83(2)	7.21(5)
0.7	7.687(9)	7.42(2)	7.396(10)	7.635(19)	7.772(15)	7.87(2)	8.23(4)	8.43(6)
0.6	10.58(2)	9.80(3)	9.562(15)	9.56(2)	9.67(2)	9.81(2)	10.08(3)	10.50(7)
0.55	14.91(4)	13.14(7)	12.26(2)	11.42(2)	11.37(2)	11.41(6)	11.60(6)	11.92(10)
0.53	18.57(6)	17.21(16)	14.95(5)	12.97(4)	12.66(5)	12.59(6)	12.44(7)	13.02(12)
0.5	25.25(6)	27.0(2)	24.57(11)	17.85(7)	16.32(13)	15.28(13)	14.39(10)	14.49(14)

TABLE VII. The measured gradient flow couplings g^2_{GF} with otherwise the same parameters as Table VI but with $c_t = 0.35$.

β_L	$L=8$	$L=10$	$L=12$	$L=16$	$L=18$	$L=20$	$L=24$	$L=30$
8	0.5911(2)	0.5808(6)	0.5771(2)	0.5727(10)	0.5739(19)	0.5734(12)	0.5739(6)	0.574(2)
6	0.8194(2)	0.8030(7)	0.7957(4)	0.7930(5)	0.7917(7)	0.7918(8)	0.7933(13)	0.804(4)
4	1.2754(5)	1.2453(16)	1.2341(8)	1.2330(8)	1.2336(13)	1.236(2)	1.245(3)	1.249(7)
3	1.7015(8)	1.659(2)	1.6533(14)	1.6575(16)	1.661(2)	1.672(3)	1.690(5)	1.711(10)
2	2.5077(16)	2.459(4)	2.462(2)	2.491(3)	2.507(3)	2.518(6)	2.549(8)	2.583(16)
1.7	2.939(2)	2.881(5)	2.897(2)	2.945(3)	2.969(6)	3.000(10)	3.045(10)	3.12(2)
1.5	3.330(2)	3.284(6)	3.294(3)	3.359(5)	3.404(5)	3.436(13)	3.502(13)	3.59(2)
1.3	3.863(3)	3.809(8)	3.833(5)	3.926(7)	3.985(11)	4.008(13)	4.083(14)	4.23(3)
1	5.174(6)	5.101(11)	5.186(7)	5.351(10)	5.451(15)	5.51(2)	5.68(4)	5.90(5)
0.9	5.906(6)	5.855(17)	5.903(10)	6.090(14)	6.21(2)	6.30(2)	6.54(3)	6.80(8)
0.8	7.005(14)	6.87(2)	6.928(11)	7.18(3)	7.30(2)	7.42(3)	7.64(5)	8.15(9)
0.7	8.946(17)	8.64(4)	8.55(2)	8.83(3)	8.96(3)	9.05(4)	9.47(7)	9.62(10)
0.6	13.12(3)	12.06(5)	11.66(2)	11.54(3)	11.62(4)	11.76(4)	12.02(6)	12.48(12)
0.55	19.72(7)	17.03(12)	15.68(4)	14.25(4)	14.09(5)	14.05(10)	14.23(11)	14.52(18)
0.53	25.51(10)	23.4(2)	19.89(8)	16.67(7)	16.11(9)	15.90(11)	15.50(12)	16.1(2)
0.5	36.17(9)	38.9(3)	35.18(18)	24.61(13)	22.0(2)	20.2(2)	18.66(18)	18.5(2)

TABLE VIII. The measured gradient flow couplings $g^2_{\rm GF}$ with otherwise the same parameters as Table VI but with $c_t = 0.4$.

β_L	$L=8$	$L=10$	$L=12$	$L=16$	$L=18$	$L=20$	$L=24$	$L=30$
8	0.5851(2)	0.5793(8)	0.5774(3)	0.5745(13)	0.576(2)	0.5770(16)	0.5779(8)	0.578(3)
6	0.8132(2)	0.8035(9)	0.7992(5)	0.7999(6)	0.7993(8)	0.7998(10)	0.8020(17)	0.814(5)
4	1.2769(6)	1.258(2)	1.2511(10)	1.2546(10)	1.2563(18)	1.260(2)	1.272(5)	1.271(9)
3	1.7227(11)	1.693(2)	1.6944(18)	1.703(2)	1.708(2)	1.721(4)	1.742(7)	1.770(13)
2	2.597(2)	2.564(6)	2.572(3)	2.609(4)	2.627(5)	2.638(9)	2.670(12)	2.70(2)
1.7	3.082(3)	3.037(7)	3.058(4)	3.115(5)	3.142(8)	3.180(14)	3.227(15)	3.30(3)
1.5	3.531(3)	3.498(10)	3.509(4)	3.583(8)	3.638(8)	3.676(18)	3.743(19)	3.84(3)
1.3	4.156(5)	4.107(12)	4.133(7)	4.241(10)	4.312(17)	4.327(19)	4.40(2)	4.59(4)
1	5.760(10)	5.66(2)	5.779(12)	5.959(15)	6.09(2)	6.13(3)	6.35(6)	6.60(8)
0.9	6.709(11)	6.66(3)	6.686(18)	6.89(2)	7.04(4)	7.12(4)	7.42(6)	7.74(13)
0.8	8.24(2)	8.03(5)	8.06(2)	8.35(6)	8.48(5)	8.62(6)	8.87(9)	9.60(18)
0.7	11.21(3)	10.70(8)	10.46(4)	10.80(7)	10.89(6)	10.95(8)	11.40(13)	11.46(18)
0.6	17.58(6)	15.98(9)	15.29(4)	14.94(6)	14.96(7)	15.07(8)	15.29(10)	15.7(2)
0.55	27.66(12)	23.5(2)	21.42(8)	18.99(8)	18.66(9)	18.48(18)	18.64(18)	18.8(3)
0.53	36.70(17)	33.6(4)	28.14(14)	22.90(13)	21.90(17)	21.4(2)	20.6(2)	21.3(3)
0.5	53.35(15)	57.8(5)	52.5(3)	35.9(2)	31.7(3)	28.7(4)	25.8(3)	25.3(4)

TABLE IX. The measured gradient flow couplings $g^2_{\rm GF}$ with otherwise the same parameters as Table VI but with $c_t = 0.45$.

β_L	$L=8$	$L=10$	$L=12$	$L=16$	$L=18$	$L=20$	$L=24$	$L=30$
8	0.5832(2)	0.5800(10)	0.5794(3)	0.5775(16)	0.580(3)	0.581(2)	0.5831(10)	0.583(3)
6	0.8142(3)	0.8079(11)	0.8060(6)	0.8095(8)	0.8094(11)	0.8100(13)	0.813(2)	0.825(7)
4	1.2935(8)	1.280(2)	1.2761(13)	1.2827(14)	1.285(2)	1.290(3)	1.307(6)	1.299(11)
3	1.7686(15)	1.744(3)	1.750(2)	1.761(2)	1.768(3)	1.782(5)	1.807(9)	1.843(17)
2	2.737(3)	2.706(9)	2.718(4)	2.762(5)	2.780(7)	2.792(13)	2.822(17)	2.86(2)
1.7	3.297(4)	3.249(10)	3.272(5)	3.335(7)	3.364(11)	3.41(2)	3.45(2)	3.53(4)
1.5	3.828(6)	3.788(14)	3.793(6)	3.874(12)	3.939(12)	3.98(2)	4.05(2)	4.17(4)
1.3	4.587(8)	4.513(19)	4.533(9)	4.657(15)	4.74(2)	4.74(2)	4.82(3)	5.05(6)
1	6.644(19)	6.48(3)	6.61(2)	6.80(2)	6.99(4)	7.00(6)	7.29(10)	7.59(14)
0.9	7.95(2)	7.87(5)	7.82(3)	8.04(4)	8.25(9)	8.30(7)	8.70(12)	9.1(2)
0.8	10.27(6)	9.85(11)	9.80(4)	10.14(11)	10.30(10)	10.43(12)	10.72(17)	11.8(3)
0.7	15.28(7)	14.20(17)	13.68(8)	14.10(15)	14.09(13)	14.07(18)	14.5(2)	14.4(3)
0.6	25.73(10)	23.15(15)	21.96(8)	21.14(10)	21.04(12)	21.07(14)	21.17(16)	21.6(3)
0.55	41.4(2)	34.9(3)	31.59(14)	27.40(14)	26.75(16)	26.3(3)	26.4(3)	26.4(5)
0.53	55.6(2)	51.1(7)	42.5(2)	33.8(2)	32.0(3)	31.2(3)	29.6(3)	30.3(6)
0.5	81.7(2)	89.6(9)	82.0(4)	55.5(3)	48.5(6)	43.4(7)	38.4(5)	37.1(7)

TABLE X. The measured gradient flow couplings $g^2_{\rm GF}$ with otherwise the same parameters as Table VI but with Wilson flow.

β_L	$L=8$	$L=10$	$L=12$	$L=16$	$L=18$	$L=20$	$L=24$	$L=30$
8	0.7777(2)	0.6961(5)	0.65497(18)	0.6141(8)	0.6053(14)	0.5977(9)	0.5894(5)	0.5828(19)
6	1.0912(2)	0.9682(6)	0.9055(3)	0.8492(4)	0.8340(5)	0.8245(6)	0.8135(10)	0.813(3)
4	1.7257(4)	1.5102(13)	1.4069(6)	1.3182(6)	1.2960(9)	1.2823(15)	1.269(2)	1.261(6)
3	2.3150(7)	2.0152(16)	1.8797(10)	1.7643(12)	1.7370(16)	1.724(2)	1.712(4)	1.706(7)
2	3.4037(13)	2.966(3)	2.7779(19)	2.623(2)	2.591(2)	2.570(4)	2.558(6)	2.554(12)
1.7	3.9705(19)	3.458(3)	3.250(2)	3.083(2)	3.050(4)	3.036(7)	3.029(7)	3.061(16)
1.5	4.4776(17)	3.919(4)	3.677(2)	3.497(3)	3.474(4)	3.456(9)	3.463(9)	3.497(17)
1.3	5.155(2)	4.517(6)	4.249(3)	4.056(5)	4.034(7)	4.009(9)	4.014(9)	4.09(2)
1	6.778(4)	5.953(7)	5.634(4)	5.418(6)	5.401(9)	5.398(14)	5.45(2)	5.56(3)
0.9	7.633(4)	6.724(11)	6.350(5)	6.105(8)	6.094(13)	6.106(15)	6.20(2)	6.33(4)
0.8	8.827(8)	7.752(15)	7.318(6)	7.068(16)	7.050(14)	7.072(19)	7.15(2)	7.42(5)
0.7	10.691(9)	9.34(2)	8.735(10)	8.413(19)	8.401(15)	8.39(2)	8.60(4)	8.66(6)
0.6	14.40(2)	12.24(3)	11.227(16)	10.50(2)	10.42(2)	10.42(2)	10.48(3)	10.69(7)
0.55	19.60(5)	16.15(8)	14.24(3)	12.46(2)	12.18(2)	12.03(6)	11.98(6)	12.01(10)
0.53	23.82(7)	20.77(18)	17.17(5)	14.05(4)	13.48(5)	13.20(6)	12.77(7)	12.97(12)
0.5	31.43(6)	31.9(2)	27.60(12)	19.01(7)	17.10(13)	15.82(13)	14.61(10)	14.25(13)

TABLE XI. The measured gradient flow couplings g^2_{GF} with otherwise the same parameters as Table VI but with the plaquette measurement of energy density.

β_L	$L=8$	$L=10$	$L=12$	$L=16$	$L=18$	$L=20$	$L=24$	$L=30$
8	0.8059(2)	0.6984(6)	0.6528(2)	0.6117(8)	0.6030(15)	0.5955(9)	0.5878(5)	0.581(2)
6	1.1209(2)	0.9649(6)	0.8986(3)	0.8434(4)	0.8289(5)	0.8204(6)	0.8102(10)	0.810(3)
4	1.7448(4)	1.4880(14)	1.3845(6)	1.3027(6)	1.2833(9)	1.2714(15)	1.260(2)	1.255(6)
3	2.3125(7)	1.9679(17)	1.8379(10)	1.7368(12)	1.7149(16)	1.705(2)	1.699(4)	1.696(7)
2	3.3486(13)	2.865(3)	2.6927(19)	2.569(2)	2.546(2)	2.533(4)	2.531(6)	2.534(12)
1.7	3.885(2)	3.328(3)	3.140(2)	3.012(2)	2.992(4)	2.988(7)	2.994(7)	3.037(16)
1.5	4.365(2)	3.758(5)	3.545(2)	3.412(3)	3.403(4)	3.397(9)	3.420(9)	3.468(17)
1.3	5.008(2)	4.316(6)	4.084(3)	3.949(5)	3.947(7)	3.935(9)	3.959(9)	4.05(2)
1	6.549(4)	5.653(7)	5.392(4)	5.262(6)	5.272(9)	5.287(14)	5.36(2)	5.50(3)
0.9	7.376(4)	6.378(11)	6.066(6)	5.921(9)	5.943(13)	5.977(15)	6.11(2)	6.26(5)
0.8	8.555(9)	7.348(16)	6.986(6)	6.851(16)	6.868(14)	6.918(19)	7.04(3)	7.35(5)
0.7	10.492(11)	8.89(2)	8.351(10)	8.16(2)	8.192(15)	8.22(2)	8.48(4)	8.59(6)
0.6	14.78(3)	11.85(4)	10.850(16)	10.25(2)	10.21(2)	10.25(2)	10.41(3)	10.73(8)
0.55	21.61(7)	16.18(9)	14.04(3)	12.29(3)	12.04(3)	11.95(6)	12.00(6)	12.22(10)
0.53	27.60(10)	21.5(2)	17.26(6)	14.00(4)	13.43(5)	13.22(7)	12.89(7)	13.37(13)
0.5	39.08(10)	35.2(3)	29.15(14)	19.43(8)	17.43(14)	16.12(13)	14.96(11)	14.91(14)

TABLE XII. The measured gradient flow couplings g^2_{GF} with otherwise the same parameters as Table VI but with the plaquette measurement of energy density and with Wilson flow.

β_L	$L=8$	$L=10$	$L=12$	$L=16$	$L=18$	$L=20$	$L=24$	$L=30$
8	1.1442(2)	0.8610(6)	0.7497(2)	0.6592(8)	0.6393(15)	0.6242(9)	0.6073(5)	0.593(2)
6	1.6195(2)	1.2003(7)	1.0377(3)	0.9115(4)	0.8809(5)	0.8616(6)	0.8381(10)	0.828(3)
4	2.5970(5)	1.8793(15)	1.6142(6)	1.4154(6)	1.3696(10)	1.3400(15)	1.307(2)	1.285(6)
3	3.5106(8)	2.5118(18)	2.1574(11)	1.8946(13)	1.8363(17)	1.802(2)	1.765(4)	1.738(7)
2	5.2024(16)	3.705(4)	3.190(2)	2.818(2)	2.738(2)	2.687(4)	2.637(6)	2.602(12)
1.7	6.086(2)	4.325(4)	3.733(2)	3.311(2)	3.223(4)	3.174(7)	3.123(7)	3.120(16)
1.5	6.882(2)	4.902(5)	4.227(2)	3.757(3)	3.671(4)	3.612(9)	3.570(9)	3.565(17)
1.3	7.954(3)	5.657(6)	4.885(3)	4.357(5)	4.265(7)	4.190(9)	4.137(9)	4.16(2)
1	10.554(5)	7.476(8)	6.484(5)	5.824(7)	5.713(9)	5.644(14)	5.61(2)	5.67(3)
0.9	11.947(6)	8.454(12)	7.313(6)	6.563(9)	6.446(13)	6.386(15)	6.39(2)	6.45(5)
0.8	13.914(10)	9.771(18)	8.436(6)	7.600(17)	7.456(15)	7.396(19)	7.38(3)	7.57(5)
0.7	17.038(14)	11.82(2)	10.083(11)	9.05(2)	8.889(15)	8.78(2)	8.87(4)	8.83(6)
0.6	23.68(4)	15.69(4)	13.037(17)	11.32(2)	11.04(2)	10.91(2)	10.83(3)	10.92(8)
0.55	33.67(10)	21.21(11)	16.71(3)	13.48(3)	12.94(3)	12.62(6)	12.39(6)	12.27(10)
0.53	42.17(14)	27.9(2)	20.37(6)	15.25(4)	14.34(5)	13.87(7)	13.22(7)	13.26(12)
0.5	58.45(14)	45.2(4)	33.94(16)	20.82(9)	18.30(14)	16.70(13)	15.14(11)	14.59(14)

TABLE XIII. The measured bare values of Z_P for each lattice size L and β_L. The step scaling mass anomalous dimension is computed from these using the steps given in the main text.

β_L	$L=8$	$L=10$	$L=12$	$L=16$	$L=18$	$L=20$	$L=24$	$L=30$
8	0.97103(6)	0.9670(2)	0.96430(10)	0.9600(3)	0.9578(6)	0.9568(3)	0.9534(2)	0.9499(6)
6	0.95990(8)	0.9545(2)	0.95067(14)	0.94396(12)	0.9413(2)	0.9405(3)	0.9358(4)	0.9298(12)
4	0.991(3)	0.9279(4)	0.9646(2)	0.9130(2)	0.9097(3)	0.9055(6)	0.9009(11)	0.893(2)
3	0.9135(2)	0.9023(5)	0.8953(3)	0.8835(4)	0.8794(4)	0.8734(9)	0.8684(12)	0.860(2)
2	0.8749(3)	0.8615(9)	0.8481(5)	0.8328(6)	0.8244(8)	0.8176(13)	0.8124(16)	0.790(3)
1.7	0.8557(4)	0.8408(11)	0.8256(6)	0.8080(8)	0.7988(8)	0.7920(16)	0.7833(18)	0.765(3)
1.5	0.8407(6)	0.8204(13)	0.8068(6)	0.7859(8)	0.7780(9)	0.7696(18)	0.754(2)	0.753(3)
1.3	0.8219(8)	0.7979(16)	0.7827(7)	0.7601(7)	0.7506(12)	0.746(2)	0.7316(19)	0.708(4)
1	0.7734(8)	0.749(2)	0.7304(10)	0.7016(17)	0.6902(18)	0.677(2)	0.664(4)	0.650(6)

(Table continued)

TABLE XIII. *(Continued)*

β_L	$L=8$	$L=10$	$L=12$	$L=16$	$L=18$	$L=20$	$L=24$	$L=30$
0.9	0.7468(10)	0.717(2)	0.7010(10)	0.6733(18)	0.660(2)	0.646(2)	0.632(2)	0.615(6)
0.8	0.703(2)	0.680(3)	0.6603(14)	0.6344(18)	0.616(2)	0.609(3)	0.595(4)	0.576(7)
0.7	0.618(2)	0.597(5)	0.588(2)	0.548(3)	0.546(3)	0.539(5)	0.515(7)	0.498(10)
0.6	0.411(2)	0.401(6)	0.376(4)	0.346(3)	0.338(9)	0.328(10)	0.293(7)	0.283(15)
0.55	0.3450(13)	0.323(4)	0.3068(16)	0.275(2)	0.267(2)	0.252(3)	0.253(5)	0.239(8)
0.53	0.3193(10)	0.299(3)	0.2842(11)	0.2619(16)	0.2514(19)	0.249(2)	0.228(2)	0.227(7)
0.5	0.2803(7)	0.254(2)	0.2425(7)	0.2356(9)	0.2345(18)	0.229(2)	0.222(2)	0.209(4)

TABLE XIV. Location of the IRFP for different discretizations: LW = Lüscher-Weisz, W = Wilson, $\tau_0 = \tau_0$correction, C = clover, and P = plaquette.

c_t	$LWC\tau_0$	LWC	LCP	WC	WP
0.3	14.5(4)	14.1(3)	14.3(2)	13.5(2)	14.0(2)
0.35	17.1(5)	17.1(2)	17.5(4)	16.1(3)	16.4(3)
0.4	22.2(6)	22.3(6)	22.9(6)	20.2(5)	20.5(5)
0.45	31(1)	31.1(9)	32(1)	27(14)	26(15)

TABLE XV. Value of γ_g^* measured from slope of the β-function for different discretizations: LW = Lüscher-Weisz, W = Wilson, $\tau_0 = \tau_0$correction, C = clover, and P = plaquette.

c_t	$LWC\tau_0$	LWC	LCP	WC	WP
0.3	0.648(97)	0.68(9)	0.74(10)	0.8(1)	0.77(10)
0.35	0.71(12)	0.699(85)	0.69(9)	0.76(12)	0.70(12)
0.4	0.73(10)	0.74(10)	0.74(10)	0.69(14)	0.59(16)
0.45	0.75(12)	0.75(11)	0.74(11)	0.51(39)	0.40(28)

TABLE XVI. Combined χ^2/d.o.f. of the beta interpolations in use (6) at different c_t and available discretization options.

c_t	$LWC\tau_0$	LWC	LCP	WC	WP
0.3	1.29	1.32	1.57	1.56	2.51
0.35	1.09	1.11	1.21	1.19	1.51
0.4	1.12	1.12	1.17	1.16	1.29
0.45	1.43	1.41	1.45	1.41	1.47

[1] C. Pica, *Proc. Sci.*, LATTICE2016 (2016) 015.
[2] D. Nogradi and A. Patella, Int. J. Mod. Phys. A **31**, 1643003 (2016).
[3] T. DeGrand, Rev. Mod. Phys. **88**, 015001 (2016).
[4] A. J. Hietanen, J. Rantaharju, K. Rummukainen, and K. Tuominen, J. High Energy Phys. 05 (2009) 025.
[5] A. J. Hietanen, K. Rummukainen, and K. Tuominen, Phys. Rev. D **80**, 094504 (2009).
[6] L. Del Debbio, A. Patella, and C. Pica, Phys. Rev. D **81**, 094503 (2010).
[7] S. Catterall, J. Giedt, F. Sannino, and J. Schneible, J. High Energy Phys. 11 (2008) 009).
[8] F. Bursa, L. Del Debbio, L. Keegan, C. Pica, and T. Pickup, Phys. Rev. D **81**, 014505 (2010).
[9] L. Del Debbio, B. Lucini, A. Patella, C. Pica, and A. Rago, Phys. Rev. D **80**, 074507 (2009).

[10] L. Del Debbio, B. Lucini, A. Patella, C. Pica, and A. Rago, Phys. Rev. D **82**, 014510 (2010).
[11] L. Del Debbio, B. Lucini, A. Patella, C. Pica, and A. Rago, Phys. Rev. D **82**, 014509 (2010).
[12] F. Bursa, L. Del Debbio, D. Henty, E. Kerrane, B. Lucini, A. Patella, C. Pica, T. Pickup, and A. Rago, Phys. Rev. D **84**, 034506 (2011).
[13] T. DeGrand, Y. Shamir, and B. Svetitsky, Phys. Rev. D **83**, 074507 (2011).
[14] A. Patella, Phys. Rev. D **86**, 025006 (2012).
[15] J. Giedt and E. Weinberg, Phys. Rev. D **85**, 097503 (2012).
[16] L. Del Debbio, B. Lucini, A. Patella, C. Pica, and A. Rago, Phys. Rev. D **93**, 054505 (2016).
[17] J. Rantaharju, T. Rantalaiho, K. Rummukainen, and K. Tuominen, Phys. Rev. D **93**, 094509 (2016).
[18] J. Rantaharju, Phys. Rev. D **93**, 094516 (2016).
[19] H. Ohki, T. Aoyama, E. Itou, M. Kurachi, C. J. D. Lin, H. Matsufuru, T. Onogi, E. Shintani, and T. Yamazaki, *Proc. Sci.*, LATTICE2010 (2010) 066.
[20] F. Bursa, L. Del Debbio, L. Keegan, C. Pica, and T. Pickup, Phys. Lett. B **696**, 374 (2011).
[21] T. Karavirta, J. Rantaharju, K. Rummukainen, and K. Tuominen, J. High Energy Phys. 05 (2012) 003.
[22] M. Hayakawa, K. I. Ishikawa, S. Takeda, M. Tomii, and N. Yamada, Phys. Rev. D **88**, 094506 (2013).
[23] T. Appelquist *et al.*, Phys. Rev. Lett. **112**, 111601 (2014).
[24] V. Leino, J. Rantaharju, T. Rantalaiho, K. Rummukainen, J. M. Suorsa, and K. Tuominen, Phys. Rev. D **95**, 114516 (2017).
[25] T. Banks and A. Zaks, Nucl. Phys. **B196**, 189 (1982).
[26] F. Herzog, B. Ruijl, T. Ueda, J. A. M. Vermaseren, and A. Vogt, J. High Energy Phys. 02 (2017) 090.
[27] Z. Fodor, K. Holland, J. Kuti, S. Mondal, D. Nogradi, and C. H. Wong, Phys. Rev. D **94**, 091501 (2016).
[28] R. Narayanan and H. Neuberger, J. High Energy Phys. 03 (2006) 064.
[29] M. Luscher, Commun. Math. Phys. **293**, 899 (2010).
[30] A. Ramos, *Proc. Sci.*, LATTICE2014 (2015) 017.
[31] S. Capitani, M. Luscher, R. Sommer, and H. Wittig (ALPHA Collaboration), Nucl. Phys. **B544**, 669 (1999).
[32] A. Patella, Phys. Rev. D **84**, 125033 (2011).
[33] S. Capitani, S. Durr, and C. Hoelbling, J. High Energy Phys. 11 (2006) 028.
[34] T. DeGrand, Y. Shamir, and B. Svetitsky, *Proc. Sci.*, LATTICE2011 (2011) 060.
[35] I. P. Omelyan, I. M. Mryglod, and R. Folk, Comput. Phys. Commun. **151**, 272 (2003).
[36] T. Takaishi and P. de Forcrand, Phys. Rev. E **73**, 036706 (2006).
[37] R. C. Brower, T. Ivanenko, A. R. Levi, and K. N. Orginos, Nucl. Phys. **B484**, 353 (1997).
[38] M. Luscher and P. Weisz, Nucl. Phys. **B479**, 429 (1996).
[39] M. Luscher and P. Weisz, J. High Energy Phys. 02 (2011) 051.
[40] M. Luscher and P. Weisz, Commun. Math. Phys. **97**, 59 (1985); **98**, 433(E) (1985).
[41] M. Lüscher, J. High Energy Phys. 08 (2010) 071; 03 (2014) 92.
[42] A. Cheng, A. Hasenfratz, Y. Liu, G. Petropoulos, and D. Schaich, J. High Energy Phys. 05 (2014) 137.
[43] P. Fritzsch and A. Ramos, J. High Energy Phys. 10 (2013) 008.
[44] Z. Fodor, K. Holland, J. Kuti, D. Nogradi, and C. H. Wong, J. High Energy Phys. 11 (2012) 007.
[45] M. Luscher, R. Sommer, P. Weisz, and U. Wolff, Nucl. Phys. **B413**, 481 (1994).
[46] Z. Fodor, K. Holland, J. Kuti, D. Nogradi, and C. H. Wong, Phys. Lett. B **779**, 230 (2018).
[47] A. Hasenfratz, D. Schaich, and A. Veernala, J. High Energy Phys. 06 (2015) 143.
[48] T. A. Ryttov and R. Shrock, Phys. Rev. D **95**, 105004 (2017).
[49] T. A. Ryttov and R. Shrock, Phys. Rev. D **95**, 085012 (2017).
[50] T. Appelquist, G. T. Fleming, and E. T. Neil, Phys. Rev. D **79**, 076010 (2009).
[51] T. DeGrand and A. Hasenfratz, Phys. Rev. D **80**, 034506 (2009).
[52] C. J. D. Lin, K. Ogawa, and A. Ramos, J. High Energy Phys. 12 (2015) 103.
[53] A. Hasenfratz and D. Schaich, J. High Energy Phys. 02 (2018) 132.
[54] M. D. Morte, R. Hoffmann, F. Knechtli, J. Rolf, R. Sommer, I. Wetzorke, and U. Wolff (ALPHA Collaboration), Nucl. Phys. **B729**, 117 (2005).
[55] J. A. M. Vermaseren, S. A. Larin, and T. van Ritbergen, Phys. Lett. B **405**, 327 (1997).
[56] T. Luthe, A. Maier, P. Marquard, and Y. Schröder, J. High Energy Phys. 01 (2017) 081.
[57] L. Giusti and M. Luscher, J. High Energy Phys. 03 (2009) 013.